

Deformed Nuclear Halos

T. Misu¹, W. Nazarewicz¹⁻³, and S. Åberg^{4,5}

¹*Department of Physics & Astronomy, University of Tennessee, Knoxville, TN 37996, U.S.A.*

²*Institute of Theoretical Physics, Warsaw University Knoxville, TN 37996, U.S.A.*

²*Institute of Theoretical Physics, Warsaw University
Hoża 69, PL-00681, Warsaw, Poland*

³*Physics Division, Oak Ridge National Laboratory
P.O. Box 2008, Oak Ridge, TN 37831, U.S.A.*

⁴*Joint Institute for Heavy Ion Research, Oak Ridge National Laboratory
P.O. Box 2008, Oak Ridge, TN 37831, U.S.A.*

⁵*Department of Mathematical Physics, Lund Institute of Technology, S-22100 Lund, Sweden.*

Abstract

Deformation properties of weakly bound nuclei are discussed in the deformed single-particle model. It is demonstrated that in the limit of a very small binding energy the valence particles in specific orbitals, characterized by a very small projection of single-particle angular momentum onto the symmetry axis of a nucleus, can give rise to the halo structure which is completely decoupled from the rest of the system. The quadrupole deformation of the resulting halo is completely determined by the intrinsic structure of a weakly bound orbital, irrespective of the shape of the core.

PACS number(s): 21.10.Dr, 21.10.Gv, 21.10.Pc, 21.60.Jz

I. INTRODUCTION

The nature of exotic nuclei with extreme isospin values is one of the most exciting challenges today, both experimentally and theoretically. Thanks to developments in experimental technology [1], we are in the process of exploring the very limits of nuclear existence, namely the regions of the periodic chart in the neighborhood of the particle drip lines. The systems of interest are characterized by extreme values of isospin corresponding to large proton or neutron excess.

On the neutron-rich side, there appears a region of loosely bound few-body systems, neutron halos (see Refs. [2–5] for reviews). In these nuclei the weak neutron binding implies large spatial dimensions and the existence of the halo (i.e., a dramatic excess of neutrons at large distances). Theoretically, the weak binding and corresponding closeness of the particle continuum, together with the need for the explicit treatment of few-body dynamics, makes the subject of halos both extremely interesting and difficult.

Neutron halos and heavy weakly bound neutron-rich nuclei offer an opportunity to study the wealth of phenomena associated with the closeness of the particle threshold: particle emission (ionization to the continuum) and characteristic behavior of cross sections [6,7], existence of soft collective modes and low-lying transition strength [8–12], and dramatic changes in shell structure and various nuclear properties in the sub-threshold regime [13–16].

In this study we address the notion of shape deformations in halo nuclei. The importance of non-spherical intrinsic shapes in halo nuclei has been stressed in some papers, especially in the context of a one-neutron halo ^{11}Be and the nucleus ^8B , alleged to be a one-proton halo. The ground state of ^{11}Be is a $1/2^+$ state. The low neutron separation energy, $S_n=504$ keV, allows for only one bound excited level ($1/2^-$ at 320 keV). The halo character of ^{11}Be has been confirmed by studies of reaction cross sections [17] and the importance of deformation can be inferred from the large quadrupole moment of its core ^{10}Be , $|Q|=229$ mb [18]. The halo character of ^8B has been suggested in Ref. [19] where the large measured quadrupole moment of its $I^\pi=2^+$ ground state, $|Q|=68$ mb, has been attributed to the weak binding of the fifth proton in the $1p_{3/2}$ state. (The existence of proton halo in ^8B is still heavily debated [3,5]. For instance, Nakada and Otsuka [20], in a shell-model calculation, demonstrated that the large value of $|Q|$ in ^8B could be understood without introducing the proton halo.)

The role of deformation in lowering the excitation energy of the $1/2^+$ intruder level in ^{11}Be has been recognized long ago. For instance, Bouten *et al.* [21] pointed out that the position of the abnormal-parity intruder orbitals in odd p -shell nuclei can be dramatically lowered by deformation, and they performed the projected Hartree-Fock calculations for the parity doublet in ^{11}Be . In another paper, based on the cranked Nilsson model, Ragnarsson *et al.* [22] demonstrated that the parity doublet could be naturally understood in terms of the $[220]1/2$ ($1d_{5/2} \otimes 2s_{1/2}$) Nilsson orbital. In particular, they calculated a very large triaxial deformation for the positive-parity level, and a less-deformed prolate shape for the negative-parity state. Muta and Otsuka [23,24] studied the structure of ^{11}Be and ^8B with a deformed Woods-Saxon potential considering quadrupole deformation as a free parameter adjusted to the data. Tanihata *et al.* [25] concluded, based on a spherical one-body potential, that the positions of experimental drip lines are consistent with the spherical picture; they emphasized the effect of increased binding of the low- ℓ shell model states near the threshold that can give rise to the level inversion. In none of these above papers, however, have both

effects, i.e., the loose binding and self-consistency been simultaneously considered.

Figure 1 shows the interaction radii for a series of Be isotopes deduced from measured interaction cross sections [26]. The relatively large radius for ^{11}Be has been interpreted as a sign for halo structure of this nucleus. It is, however, quite interesting to note that calculated deformations (as obtained in Nilsson-Strutinsky calculations) of the Be isotopes are found to vary in such a way that the corresponding nuclear radii reproduce the data quite well. In this case, no effects from the halo structure of ^{11}Be have been considered since the calculations are based on the modified oscillator potential. Although these calculations are somewhat unrealistic, the result displayed in Fig. 1 clearly stresses the importance of simultaneously considering both deformation and halo effects as, e.g., in ^{11}Be .

Another, more microscopic, approach is the work by Kanada-En'yo *et al.* [27] based on antisymmetrized molecular dynamics with improved asymptotics. They obtained very large quadrupole deformation for the $1/2^+$ state in ^{11}Be , and a less deformed $1/2^-$ state. A similar conclusion has been drawn in the recent self-consistent Skyrme-Hartree-Fock calculations [28].

Also, very recently, the notion of deformation in ^{11}Be has been pursued by several authors [29–33] within several variants of the weak coupling scheme. In these models, the odd neutron moving in a Woods-Saxon potential is weakly coupled to the deformed core of ^{10}Be , and interacts with the core through the quadrupole field. The deformation of ^{11}Be is not treated self-consistently; either the strength of the quadrupole coupling is adjusted to the data to reproduce the quadrupole moment of ^{10}Be , or the deformation is adjusted to reproduce the energies of the $I=1/2$ doublet. The advantage of the weak coupling approach is that the total wave functions are eigenstates of the total angular momentum and they have correct asymptotic behavior. In this context, a nice molecular analogy, in which the adiabatic coupling of the valence particle to the deformed core is applied, is the weak binding of an electron to a rotationally excited dipolar system [34], or to a neutral symmetric molecule with a non-zero quadrupole moment [35].

In this study, we address the question of deformed two-body halos by considering the single-particle motion in the axial spheroidal square well. The corresponding Schrödinger equation can be separated into three ordinary differential equations in the spheroidal coordinate system. The properties of the deformed single-particle states, especially in the subthreshold region, are analyzed by making the multipole decomposition in the spherical partial waves with well-defined orbital angular momentum. Large spatial extensions of deformed halos are discussed in terms of spherical radial form-factors.

The paper is organized as follows. Section II contains the discussion of the generic properties of deformed halos. The method of evaluation of the prolate spheroidal wave functions is described in Sec. III, and the results of calculations are discussed in Sec. IV. Finally, Sec. V contains the main conclusions of the paper.

II. DEFORMED NEUTRON HALOS, GENERAL PROPERTIES

This section contains some general arguments regarding the concept of shape deformation in two-body halo systems. The material contained in this section is the extension of the analysis of Ref. [36] carried out for the spherical case. (For the corresponding discussion of three-body halo asymptotics, see Ref. [37].)

Let us assume that the weakly bound neutron moves in a deformed average potential $U(\mathbf{r})$ (usually well approximated by a sum of the central potential and the spin-orbit potential). The neutron wave function can be obtained by solving the deformed single-particle Schrödinger equation

$$\left[\nabla^2 - \frac{2m}{\hbar^2} U(\mathbf{r}) - \kappa_\nu^2 \right] \psi_\nu(\mathbf{r}) = 0, \quad (1)$$

where $\kappa_\nu = \sqrt{-2m\epsilon_\nu/\hbar^2}$ and ϵ_ν is the corresponding single-particle energy ($\epsilon_\nu < 0$).

In the following considerations we assume the axial reflection-symmetric central potential. (The generalization to the triaxial and/or reflection-asymmetric case is straightforward.) Since the asymptotic properties of radial matrix elements depend very weakly on intrinsic spin, the spin-orbit term is neglected. Thanks to the axial symmetry, the single-particle states are labeled by means of Λ - the projection of the single-particle angular momentum onto the symmetry axis (z -axis) and parity, π . Since the Hamiltonian considered is invariant with respect to the time-reversal symmetry, we shall only consider non-negative values of Λ .

The deformed wave function can be decomposed into spherical partial waves with the well-defined orbital angular momentum ℓ :

$$\psi_\nu^\Lambda(\mathbf{r}) = \sum_\ell R_{\ell\Lambda\nu}(r) Y_{\ell\Lambda}(\hat{\mathbf{r}}), \quad (2)$$

where, due to the assumed reflection symmetry,

$$\pi = (-1)^\ell. \quad (3)$$

At large distances ($r > R$, where R defines the arbitrary but fixed distance at which the nuclear interaction becomes unimportant), $U(\mathbf{r})$ vanishes and the radial functions $R_{\ell\nu}(r)$ satisfy the free-particle radial Schrödinger equation

$$\left[\frac{d^2}{dr^2} + \frac{2}{r} \frac{d}{dr} - \kappa_\nu^2 - \frac{\ell(\ell+1)}{r^2} \right] R_{\ell\nu}(r) = 0. \quad (4)$$

(Of course, $R_{\ell\Lambda\nu}(r) = R_{\ell\nu}(r)$ for $r \geq R$.) The solution of Eq. (4) is $R_{\ell\nu}(r) = B_\ell h_\ell^+(i\kappa_\nu r)$ where h_ℓ^+ is the spherical Hankel function and B_ℓ is a constant, given by

$$B_\ell = R_{\ell\nu}(R)/h_\ell^+(i\kappa_\nu R). \quad (5)$$

The spatial properties of the system can be characterized by radial moments, $\langle \psi_\nu^\Lambda | r^n | \psi_\nu^\Lambda \rangle$, and multipole moments $\langle \psi_\nu^\Lambda | r^n Y_{n0} | \psi_\nu^\Lambda \rangle$. Both quantities require the evaluation of radial matrix elements

$$\langle \ell\Lambda\nu | r^n | \ell'\Lambda\nu \rangle \equiv \int_0^\infty r^{n+2} R_{\ell\Lambda\nu}^*(r) R_{\ell'\Lambda\nu}(r) dr = I_{n\ell\ell'\Lambda\nu} + O_{n\ell\ell'\nu}, \quad (6)$$

where I represents the contribution from the inner ($r < R$) region and O is the outer region contribution ($r > R$). Thanks to parity conservation [Eq. (3)], $\ell' = \ell \bmod 2$. The inner integral is, by definition, finite. The outer integral can be written as

$$O_{n\ell\ell'\nu} = \int_R^\infty r^{n+2} B_\ell^* B_{\ell'} h_\ell^{+*}(i\kappa_\nu r) h_{\ell'}^+(i\kappa_\nu r) dr \quad (7)$$

$$= B_\ell^* B_{\ell'} \kappa_\nu^{-(n+3)} \int_{R\kappa_\nu}^\infty h_\ell^{+*}(ix) h_{\ell'}^+(ix) x^{n+2} dx. \quad (8)$$

In the limit of a very weak binding ($\kappa_\nu \rightarrow 0$) one can replace the value of $h_\ell^+(i\kappa_\nu R)$ in Eq. (5) by the asymptotic expression valid for small arguments. This gives:

$$B_\ell \approx \frac{i^{\ell+1}}{1 \times 3 \times \dots (2\ell - 1)} R_{\ell\nu}(R) (R\kappa_\nu)^{\ell+1}. \quad (9)$$

Now, following the arguments of Ref. [36], one can demonstrate that for small values of κ_ν , $O_{n\ell\ell'\nu}$ behaves asymptotically as

$$O_{n\ell\ell'\nu} \propto \kappa_\nu^{\ell+\ell'-n-1} \left\{ \frac{x_0^{n-\ell-\ell'+1} - (R\kappa_\nu)^{n-\ell-\ell'+1}}{n - \ell - \ell' + 1} + \text{const.} \right\}, \quad (10)$$

where $x_0 \gg R\kappa_\nu$ is a small constant. Consequently, the asymptotic behavior of $O_{n\ell\ell'\nu}$ in the limit of small ϵ strongly depends on quantum numbers n , ℓ , and ℓ' . Namely, for

$$n > \ell + \ell' - 1 : O_{n\ell\ell'\nu} \text{ diverges as } (-\epsilon_\nu)^{(\ell+\ell'-n-1)/2}, \quad (11)$$

$$n = \ell + \ell' - 1 : O_{n\ell\ell'\nu} \text{ diverges as } -\frac{1}{2} \ln(-\epsilon_\nu), \quad (12)$$

$$n < \ell + \ell' - 1 : O_{n\ell\ell'\nu} \text{ remains finite.} \quad (13)$$

A. The normalization integral

The norm of the deformed state [Eq (2)], $\mathcal{N}_{\Lambda\nu}$, can be expressed through the zeroth radial moment

$$(\mathcal{N}_{\Lambda\nu})^2 = \langle \psi_\nu^\Lambda | \psi_\nu^\Lambda \rangle = \sum_\ell \langle \ell\Lambda\nu | r^0 | \ell\Lambda\nu \rangle = \sum_\ell (I_{0\ell\ell\Lambda\nu} + O_{0\ell\ell\nu}). \quad (14)$$

Consequently, according to Eq. (11), the norm is divergent only if the deformed state contains an admixture of the s -wave. This is possible only for orbitals with $\pi=+$ and $\Lambda=0$. In this case, the norm behaves asymptotically as $\sqrt{O_{000\nu}} \propto (-\epsilon_\nu)^{-1/4}$, and the probability to find the neutron in the outer region,

$$P_{\text{outer}} = \frac{O}{I + O}, \quad (15)$$

approaches one for zero binding.

B. The rms radius

The root-mean-square radius of a deformed orbital is given by

$$\langle \Lambda\nu | r^2 | \Lambda\nu \rangle \equiv \frac{\langle \psi_\nu^\Lambda | r^2 | \psi_\nu^\Lambda \rangle}{\langle \psi_\nu^\Lambda | \psi_\nu^\Lambda \rangle} = (\mathcal{N}_{\Lambda\nu})^{-2} \sum_\ell \langle \ell \Lambda\nu | r^2 | \ell \Lambda\nu \rangle. \quad (16)$$

As discussed in Ref. [36], with decreasing binding energy the integral $O_{2\ell\ell\nu}$ diverges as $(-\epsilon_\nu)^{-3/2}$ for $\ell=0$ and as $(-\epsilon_\nu)^{-1/2}$ for $\ell=1$ [see Eq. (11)]. Therefore, in the deformed system, the rms radius diverges only if the Nilsson orbital in question contains a component of an s or a p state. This leaves only three classes of states for which the spatial extension can be arbitrary large:

$$\begin{aligned} \pi = +, \Lambda = 0 : \quad \langle r^2 \rangle \text{ diverges as } (-\epsilon_\nu)^{-1}, \\ \pi = -, \Lambda = 0 \text{ or } 1 : \langle r^2 \rangle \text{ diverges as } (-\epsilon_\nu)^{-1/2}. \end{aligned} \quad (17)$$

In the following, these states are referred to as ‘‘halo states’’ or ‘‘halos’’. Of course, this does not mean that other Nilsson orbitals cannot form very extended structures when their binding becomes very small. However, it is only for the states (17) that the rms radius becomes infinite asymptotically.

C. The quadrupole moment

The average quadrupole moment of a deformed orbital is given by

$$\langle \Lambda\nu | r^2 Y_{20} | \Lambda\nu \rangle = \frac{\langle \psi_\nu^\Lambda | r^2 Y_{20} | \psi_\nu^\Lambda \rangle}{\langle \psi_\nu^\Lambda | \psi_\nu^\Lambda \rangle} = (\mathcal{N}_{\Lambda\nu})^{-2} \sum_{\ell\ell'} \langle \ell \Lambda\nu | r^2 | \ell' \Lambda\nu \rangle \langle \ell \Lambda | Y_{20} | \ell' \Lambda \rangle, \quad (18)$$

where the angular matrix element is

$$\langle \ell \Lambda | Y_{20} | \ell' \Lambda \rangle = \sqrt{\frac{5}{4\pi}} \sqrt{\frac{2\ell' + 1}{2\ell + 1}} \langle \ell' \Lambda 20 | \ell \Lambda \rangle \langle \ell' 0 20 | \ell 0 \rangle. \quad (19)$$

According to Eq. (11), in the $\epsilon_\nu \rightarrow 0$ limit the quadrupole matrix element diverges if $\ell + \ell' < 3$. Since the quadrupole moment of an s state vanishes, the only diverging matrix element among the $\pi=+$ states comes from an $s \leftrightarrow d$ coupling. At small binding energies, the corresponding integral $O_{202\nu}$ behaves as $(-\epsilon_\nu)^{-1/2}$. For negative-parity orbitals, the only diverging matrix element is the diagonal one, $O_{211\nu}$, which also behaves as $(-\epsilon_\nu)^{-1/2}$.

However, because of different asymptotic properties of the normalization integrals, the low- ϵ behavior of the single-particle quadrupole moment of a weakly bound orbital does depend on parity. With $\epsilon_\nu \rightarrow 0$, the quadrupole moment (18) of the $\pi=+$ halo approaches the finite limit. On the other hand, for the $\pi=-$ halos the norm of the state remains finite and the quadrupole moment behaves as $(-\epsilon_\nu)^{-1/2}$.

It is instructive to consider the quadrupole deformation β_2 extracted from the ratio

$$\beta_2 \equiv \frac{4\pi}{5} \frac{\langle r^2 Y_{20} \rangle}{\langle r^2 \rangle}. \quad (20)$$

By splitting $\langle r^2 Y_{20} \rangle$ and $\langle r^2 \rangle$ into contributions from the core (c) and from the valence (v) nucleons, one obtains

$$\beta_2 = \frac{4\pi}{5} \frac{\langle r^2 Y_{20} \rangle_c + \langle r^2 Y_{20} \rangle_v}{\langle r^2 \rangle_c + \langle r^2 \rangle_v}. \quad (21)$$

For positive-parity halos ($\pi=+$, $\Lambda=0$), the numerator in Eq. (21) is finite while the denominator diverges as $(-\epsilon_\nu)^{-1}$. Hence β_2 is asymptotically linear in ϵ_ν , i.e., it *vanishes* in the limit of zero binding:

$$\beta_2(\pi = +, \Lambda = 0) \xrightarrow{\epsilon_\nu \rightarrow 0} 0. \quad (22)$$

On the other hand, for negative-parity halos ($\pi=-$, $\Lambda=0$ or 1), the ratio (21) is solely determined by the p -wave components in the valence state:

$$\beta_2(\pi = -, \Lambda) \xrightarrow{\epsilon_\nu \rightarrow 0} \frac{4\pi}{5} \langle 1\Lambda | Y_{20} | 1\Lambda \rangle = \begin{cases} +0.63 & \text{if } \Lambda = 0 \\ -0.31 & \text{if } \Lambda = 1. \end{cases} \quad (23)$$

That is, the deformation of the halo is solely determined by the spatial structure of the valence state wave function, independently of the shape of the core. The deformed core merely establishes the quantization axis of the system, important for determining the projection Λ .

D. Higher moments and multipole deformations

The above discussion is easily generalized to the case of higher multipoles. For instance, for $n=4$, the hexadecapole moment $\langle r^4 Y_{40} \rangle$ behaves asymptotically in the same manner as the quadrupole moment, i.e., it approaches the finite limit for the $\pi=+$ halos and diverges as $(-\epsilon_\nu)^{-1/2}$ for the $\pi=-$ halos. However, the corresponding deformation β_4 , proportional to $\langle r^4 Y_{40} \rangle / \langle r^4 \rangle$ approaches zero, regardless of parity of the halo orbital.

III. THE MODEL

In our study, the deformed potential $U(\mathbf{r})$ has been approximated by a prolate spheroidal finite square well potential. Spheroidal *infinite* square well was early used by Moszkowski [38] to discuss the properties of single-particle deformed orbitals. Merchant and Rae [39] investigated the continuum spectrum ($\epsilon>0$) of the spheroidal finite square well potential to calculate the particle decay widths of deformed nuclei. Since the main focus of our work is the behavior of bound single-particle orbitals very close to the $\epsilon=0$ threshold, particular attention was paid to a precise numerical solution of the Schrödinger equation in the limit of very small binding energies and/or large deformations.

A. Prolate Spheroidal Coordinates and Parametrization of Nuclear Shape

Assuming the z -axis to be a symmetry axis of the nucleus, the coordinate transformation between the prolate spheroidal coordinates (ξ, η, ϕ) and the cartesian coordinates (x, y, z) reads [40–42]:

$$x = a\sqrt{(\xi^2 - 1)(1 - \eta^2)} \cos \phi, \quad (24)$$

$$y = a\sqrt{(\xi^2 - 1)(1 - \eta^2)} \sin \phi, \quad (25)$$

$$z = a\xi\eta, \quad (26)$$

where $a > 0$, $1 \leq \xi \leq \infty$, $-1 \leq \eta \leq 1$, and $0 \leq \phi \leq 2\pi$.

Surfaces of constant $\xi = \xi_0$ represent confocal ellipses,

$$\frac{x^2 + y^2}{a^2(\xi_0^2 - 1)} + \frac{z^2}{a^2\xi_0^2} = 1, \quad (27)$$

with foci at $(0, 0, \pm a)$, minor axis $R_{\perp} = a\sqrt{\xi_0^2 - 1}$, and major axis $R_{\parallel} = a\xi_0$. (Since the purpose of this study is to investigate the generic features of weakly bound states in a deformed potential, the analysis is limited to prolate shapes. However, the calculations can easily be extended to the oblate side through a simple coordinate transformation.)

It is seen from Eq. (27) that the parameter ξ_0 defines the shape deformation of a system. Indeed, for $\xi_0 \gg 1$, the surface (27) becomes that of a sphere with the radius $a\xi_0$, while the limit $\xi_0 \rightarrow 1$ corresponds to a segment. Following Ref. [38], we introduce the deformation parameter δ :

$$\delta = \left(\frac{R_{\parallel}}{R_{\perp}}\right)^{2/3} - 1 = \left(\frac{\xi_0^2}{\xi_0^2 - 1}\right)^{1/3} - 1. \quad (28)$$

The volume-conservation condition [the volume inside the surface (27) should not depend on δ] yields

$$a = \frac{R_0}{(\xi_0^3 - \xi_0)^{1/3}}, \quad (29)$$

where R_0 is the corresponding spherical radius.

To find the relation between δ and other quadrupole deformation parameters, one can compare the macroscopic quadrupole moment of the surface (27)

$$Q_2 = \sqrt{\frac{16\pi}{5}} \langle r^2 Y_{20} \rangle = \frac{2}{5} R_0^2 \delta \frac{\delta^2 + 3\delta + 3}{\delta + 1} \quad (30)$$

with those obtained using other shape parametrizations [43]. For example, the relation between δ and the oscillator deformation δ_{osc} is

$$\delta = \left(\frac{1 + \frac{1}{3}\delta_{\text{osc}}}{1 - \frac{2}{3}\delta_{\text{osc}}}\right)^{2/3} - 1. \quad (31)$$

For small values of δ_{osc} , Eq. (31) gives $\delta = \frac{2}{3}\delta_{\text{osc}}$. However, at a superdeformed shape ($\frac{R_{\parallel}}{R_{\perp}} = 2$), both deformations are very close: $\delta_{\text{osc}} = 0.6$ while $\delta = 2^{2/3} - 1 = 0.587$. Figure 2 shows the family of shapes representing different deformations δ .

B. Bound States in the Prolate Spheroidal Well

The deformed spheroidal square well potential is given by

$$U(\xi) = \begin{cases} U_0 & \text{for } \xi \leq \xi_0 \\ 0 & \text{for } \xi > \xi_0, \end{cases} \quad (32)$$

where U_0 is the depth of the potential well ($U_0 < 0$) and ξ_0 depends on δ through Eq. (28).

Expressed in prolate spheroidal coordinates, the time-independent Schrödinger equation (1) can be written as

$$\left[\frac{\partial}{\partial \xi} \left\{ (\xi^2 - 1) \frac{\partial}{\partial \xi} \right\} + \frac{\partial}{\partial \eta} \left\{ (1 - \eta^2) \frac{\partial}{\partial \eta} \right\} + \frac{\xi^2 - \eta^2}{(\xi^2 - 1)(1 - \eta^2)} \frac{\partial^2}{\partial \phi^2} \right] \psi(\xi, \eta, \phi) + \frac{2ma^2(\eta^2 - \xi^2)}{\hbar^2} [U(\xi) - \epsilon] \psi(\xi, \eta, \phi) = 0. \quad (33)$$

Following Ref. [40], this equation can be separated into three ordinary differential equations by assuming $\psi(\xi, \eta, \phi) = R(\xi)S(\eta)\Phi(\phi)$. The functions R , S , and Φ are solutions of the ordinary differential equations

$$\frac{d}{d\xi} \left[(\xi^2 - 1) \frac{dR_{\Lambda}(c, \xi)}{d\xi} \right] - \left[\lambda_{\Lambda} - c^2 \xi^2 + \frac{\Lambda^2}{\xi^2 - 1} \right] R_{\Lambda}(c, \xi) = 0, \quad (34)$$

$$\frac{d}{d\eta} \left[(1 - \eta^2) \frac{dS_{\Lambda}(c, \eta)}{d\eta} \right] + \left[\lambda_{\Lambda} - c^2 \eta^2 - \frac{\Lambda^2}{1 - \eta^2} \right] S_{\Lambda}(c, \eta) = 0, \quad (35)$$

$$\frac{d^2 \Phi_{\Lambda}(\phi)}{d\phi^2} = -\Lambda^2 \Phi_{\Lambda}(\phi), \quad (36)$$

where λ_{Λ} is the separation constant and

$$c = \begin{cases} c_{\text{int}} = a\sqrt{2m(\epsilon - U_0)}/\hbar & \text{for } \xi \leq \xi_0 \\ ic_{\text{ext}} = ia\sqrt{-2m\epsilon}/\hbar & \text{for } \xi > \xi_0. \end{cases} \quad (37)$$

In the following, $R_{\Lambda}(c, \xi)$ and $S_{\Lambda}(c, \eta)$ are referred to as the radial and angular spheroidal functions, respectively. For positive values of ϵ , scattering solutions for the spheroidal square well were solved in Ref. [39]. Here, we concentrate on bound states with $\epsilon < 0$.

The angular solution $S_{\Lambda}(c, \eta)$ can be expressed in terms of a series of the associated Legendre functions of the first kind

$$S_{\Lambda}(c, \eta) = \sum_k^{\infty'} d_k^{\Lambda}(c) P_{\Lambda+k}^{\Lambda}(\eta), \quad (38)$$

where the prime over the summation sign indicates that $k=0, 2, \dots$ if $(l - \Lambda)$ is even, and $k=1, 3, \dots$ if $(l - \Lambda)$ is odd [40,42] (parity conservation).

The radial functions $R_{\Lambda}(c, \xi)$ are expanded in terms of spherical Bessel functions of the first kind, $f_k^{(1)}(c\xi) \equiv j_k(c\xi)$, and spherical Bessel functions of the third kind $f_k^{(3)}(c\xi) \equiv h_k(c\xi) = j_k(c\xi) + in_k(c\xi)$. The internal radial function $R_{\Lambda}^{(1)}(c, \xi)$ ($\xi \leq \xi_0$) and the external radial function $R_{\Lambda}^{(3)}(c, \xi)$ ($\xi > \xi_0$) can be written as

$$R_{\Lambda}^{(p)}(c, \xi) = \left\{ \sum_k^{\infty'} \frac{(2\Lambda + k)!}{k!} d_k^{\Lambda}(c) \right\}^{-1} \left(\frac{\xi^2 - 1}{\xi^2} \right)^{\Lambda/2} \sum_k^{\infty'} i^{k+\Lambda-l} \frac{(2m+k)!}{k!} d_k^{\Lambda}(c) f_{\Lambda+k}^{(p)}(c\xi) \quad (39)$$

where $p=1$ or 3 .

Finally, the deformed single-particle wave function is given by

$$\psi_{\Lambda n_{\text{exc}}}(\xi, \eta, \phi) = \begin{cases} \sum_l^{\infty} A_{n_{\text{exc}}\Lambda l} R_{\Lambda l}^{(1)}(c_{\text{int}}, \xi) S_{\Lambda l}(c_{\text{int}}, \eta) \Phi_{\Lambda}(\phi) & \text{for } \xi \leq \xi_0 \\ \sum_l^{\infty} B_{n_{\text{exc}}\Lambda l} R_{\Lambda l}^{(3)}(ic_{\text{ext}}, \xi) S_{\Lambda l}(ic_{\text{ext}}, \eta) \Phi_{\Lambda}(\phi) & \text{for } \xi > \xi_0 \end{cases} \quad (40)$$

where c_{int} and c_{ext} are defined in Eq. (37), and n_{exc} is the excitation quantum number labeling orbitals having the same quantum numbers Λ and $\pi=(-1)^l$.

By matching the internal and external wave functions at $\xi=\xi_0$, one finds the eigenenergies ϵ and the amplitudes $A_{n_{\text{exc}}\Lambda l}$ and $B_{n_{\text{exc}}\Lambda l}$. The details of the calculation are outlined in Appendix A. The procedure used to calculate the separation constant $\lambda_{\Lambda l}$ and coefficients $d_k^{\Lambda}(c)$ is discussed in Appendix B.

IV. RESULTS

This section illuminates the general properties of deformed Nilsson orbitals discussed in Sec. II using the spheroidal square well potential.

The single-particle energies of the finite spheroidal well with $U_0=-80$ MeV and $R_0=4$ fm are shown in Fig. 3 as functions of deformation δ . At a spherical shape the orbitals are characterized by means of spherical quantum numbers $(n\ell)$. The deformed orbitals are labeled by parity π , angular momentum projection Λ , and the excitation quantum number n_{exc} which specifies the energetic order of a single-particle orbital in a given $(\pi\Lambda)$ -block, counting from the bottom of the well (e.g., $n_{\text{exc}}=1$ corresponds to the lowest state, $n_{\text{exc}}=2$ is the second state, and so on). In the following, the deformed orbitals are labeled as $[n_{\text{exc}}\Lambda\pi]$. For example, the $\Lambda=1$ orbital originating from the spherical shell $1d$ is referred to as $[11+]$ (see Fig. 3).

A. Radial Properties of Deformed Orbitals

The dependence of the single-particle rms radius on binding energy is illustrated in Fig. 4 (spherical shape), and Figs. 5 and 6 (superdeformed shape). (In calculations, the binding energy was varied by changing the well depth U_0 .)

The spherical case has been discussed in detail in Ref. [36]; here it is shown for the mere reference only. In all cases the asymptotic conditions [Eq. (17)] are met rather quickly. Indeed, in the considered range of binding energy the values of $\langle r^2 \rangle$ for the $1s$ state shown in Fig. 4 and the $[10+]$, $[20+]$, and $[30+]$ orbitals of Fig. 5 approach an asymptotic limit [$(-\epsilon)^{-1}$ dependence], and similar holds for the $1p$ state and $[10-]$, $[20-]$, $[11-]$, and $[21-]$ orbitals (see Fig. 6) which behave as $(-\epsilon)^{-1/2}$ at low binding energy. The remaining states do not exhibit any halo effect, as expected.

Figure 7 displays the probability P_{outer} [Eq. (15)] to find the neutron in the classically forbidden region, $\xi > \xi_0$, as a function of ϵ for three superdeformed states with different

values of Λ . At low values of binding energy, the $\ell=0$ component completely dominates the structure of the $[20+]$ state and $P_{\text{outer}} \rightarrow 1$.

The radial form factors $R_{\ell\Lambda n_{\text{exc}}}(r)$ appearing in the multipole decomposition [Eq. (2)] carry information about the spatial extension of the wave function. They can be obtained by the angular integration:

$$R_{\ell\Lambda n_{\text{exc}}}(r) = \int \psi_{n_{\text{exc}}\pi}^{\Lambda}(\mathbf{r}) Y_{\ell\Lambda}^*(\hat{\mathbf{r}}) d\hat{\mathbf{r}}. \quad (41)$$

Since in our calculations the total wave function $\psi_{n_{\text{exc}}\pi}^{\Lambda}(\mathbf{r})$ is normalized to unity, the integral

$$P_{\ell}(\Lambda n_{\text{exc}}) \equiv \int_0^{\infty} |R_{\ell\Lambda n_{\text{exc}}}(r)|^2 r^2 dr \quad (42)$$

represents the probability to find the partial wave ℓ in the state $[n_{\text{exc}}\Lambda\pi]$. Of course,

$$\sum_{\ell} P_{\ell}(\Lambda n_{\text{exc}}) = 1. \quad (43)$$

Figures 8 and 9 display the radial formfactors for several orbitals in a superdeformed well assuming the subthreshold binding energy of $\epsilon=-5$ keV. For the $\pi=+$, $\Lambda=0$ orbitals (Fig. 8), the $\ell=0$ component dominates at this extremely low binding energy, in spite of a very large deformation. Indeed, according to the discussion in Sect. II A, the value of $P_{\ell=0}(0n_{\text{exc}})$ approaches one at small binding energies. In other words, the $\pi=+$, $\Lambda=0$ halos behave at low values of ϵ like s waves. It is interesting to note that both the $[20+]$ and $[30+]$ orbitals are dominated by the $2s$ component; the corresponding $\ell=0$ form factors have only one node. For the $\pi=-$ halo orbitals with $\Lambda=0$ and 1 (Fig. 9), the p component does not dominate the wave function completely (Sect. II A), but a significant excess of a p wave at large distances is clearly seen. The radial decomposition of other orbitals ($\Lambda > 1$), shown in Figs. 8 and 9, very weakly depends on binding energy; it reflects the usual multipole mixing due to the deformed potential.

The results presented in Figs. 8 and 9 illustrate the fact that the multipole decomposition of the deformed level depends on *both* deformation and the binding energy. Figures 10 ($\pi=+$) and 11 ($\pi=-$) show contour maps of $P_{\ell}(\Lambda n_{\text{exc}})$ for the $\Lambda=0$ orbitals as functions of ϵ and δ . The structure of the $[10+]$ level, originating from the spherical $1s$ state, is completely dominated by the $\ell=0$ component, even at very large deformations. A rather interesting pattern is seen in the diagram for the $[20+]$ orbital originating from the spherical $1d$ state. The $\ell=2$ component dominates at low and medium deformations, and the corresponding probability $P_{\ell=2}$ slowly decreases with δ , at large deformations approaching the (constant) asymptotic limit. However, a similar effect, namely the decrease of the $\ell=2$ component, is seen when approaching the $\epsilon=0$ threshold. In the language of the perturbation theory [7], this rapid transition comes from the coupling to the low-energy $\ell=0$ continuum; the $\ell=0$ form factor of the $[20+]$ orbital shows, at low values of ϵ , a one-nodal structure characteristic of the $2s$ state (see Fig. 8). At low deformations, the amplitude of the s component in the $[20+]$ state is proportional to δ . Remembering that the norm, Eq. (14), behaves as $(-\epsilon)^{-1/4}$ for the $\ell=0$ state, one can conclude that at low values of δ and ϵ the contours of constant $P_{\ell=0}$ correspond to the power law $\delta^2 \propto (-\epsilon)^{1/2}$. This result, seen in Fig. 10, tells us that the s component takes over very quickly even if deformation δ is small. (A similar conclusion for the $1/2^+$ ground state of ^{11}Be has been reached in Ref. [33].)

The partial-wave probabilities calculated for the negative parity states [10−] and [20−] presented in Fig. 11 do not show such a dramatic rearrangement around the threshold. Namely, the [10−] orbital retains its $\ell=1$ structure in the whole deformation region considered, and the structure of the [20−] state at large deformations can be viewed in terms of a mixture of p and f waves. In the latter case there is a clear tendency to increase the $\ell=1$ contribution at low binding energies, but this effect is much weaker compared to the [20+] case discussed above.

B. Quadrupole Moments and Deformations

Deformation properties of single-particle orbitals, namely the intrinsic quadrupole moments $\langle r^2 Y_{20} \rangle$ and quadrupole deformations β_2 , Eq. (20), are displayed in Figs. 5 and 6 as functions of binding energy at $\delta=0.6$ (superdeformed shape). It is seen that the asymptotic limits discussed in Sec. II are reached at low values of ϵ in practically all cases. In particular, the values of β_2 for the $\pi=+$, $\Lambda=0$ orbitals approach zero with $\epsilon \rightarrow 0$ [Eq. (22)], those for the $\pi=-$, $\Lambda=0$ states approach the limit of 0.63, and the value of β_2 for the [11−] orbital is close to the value of -0.31 [see Eq. (23)]. The only exception is the [21−] orbital which at deformation $\delta=0.6$ contains only 31% of the $\ell=1$ component (see Fig. 9); hence the positive contribution of the $1f$ state to $\langle r^2 Y_{20} \rangle$ still dominates.

To illustrate the interplay between the core deformation and that of the valence particle [Eq. (21)], we display in Figs. 12 and 13: (i) quadrupole deformation β_2 of the valence orbital, (ii) quadrupole deformation of the core, and (iii) total quadrupole deformation of the system. Here we assume that the core consists of *all* single-particle orbitals lying energetically below the valence orbital, and that each state (including the valence one) is occupied by two particles. It is convenient to rewrite Eq. (21) in the form:

$$\beta_{2,\text{tot}} = \frac{\beta_{2,c} \langle r^2 \rangle_c + \beta_{2,v} \langle r^2 \rangle_v}{\langle r^2 \rangle_c + \langle r^2 \rangle_v} = \frac{\beta_{2,v} + \chi \beta_{2,c}}{1 + \chi}, \quad (44)$$

where

$$\chi \equiv \frac{\langle r^2 \rangle_c}{\langle r^2 \rangle_v}. \quad (45)$$

For the halo states, $\chi \rightarrow 0$ and $\beta_{2,\text{tot}} \rightarrow \beta_{2,v}$. The results shown in Figs. 12 and 13 nicely illustrate this behavior. Namely, for very small binding energy the total deformation of the system coincides with that of valence, *regardless* of the core deformation. These results illustrate the deformation decoupling of the deformed halo from the rest of the system. A nice example of this decoupling has been discussed by Muta and Otsuka [23], who demonstrated that the halo proton in ${}^8\text{B}$ occupying the $1p_{3/2}$, $\Lambda=1$ weakly bound orbit produces the oblate density distribution which greatly reduces the large quadrupole moment of the prolate core.

C. Deformation Softness of Halo Systems in the Mean-Field Calculations

The effect of decoupling of the valence particles from the deformed core in the limit of a very weak binding suggests that in such cases the constrained Hartree-Fock (CHF) or

Nilsson-Strutinsky (NS) calculations would produce very shallow potential energy surfaces. Indeed, in the CHF theory the nuclear Hamiltonian H is minimized under the constraint that the multipole operator that defines the intrinsic shape has a fixed expectation value $\langle Q \rangle = q$. The intrinsic wave functions are found by minimizing the Routhian

$$H' = H - \beta Q, \quad (46)$$

where β is the corresponding Lagrange multiplier. If Q is the quadrupole moment and the nucleus is weakly bound, then, especially in the case of halo systems, $\langle Q \rangle$ is very sensitive to small variations in the single-particle energy ϵ_ν of the last occupied single-particle orbital. In particular, for the $\pi=-$ halos, $\langle Q \rangle$ can take practically any value without changing the HF energy $\langle H \rangle$. This means that the numerical procedure used for searching for the self-consistent solution can be rather susceptible to uncontrolled variations of q with ϵ_ν .

In the Nilsson-Strutinsky calculations, the bulk part of the binding energy comes from the the macroscopic energy E_{macro} . Commonly used is the Yukawa-plus-exponential macroscopic energy formula [44] which accounts for the surface thickness. The corresponding generalized surface energy reads

$$E_s = -\frac{c_s}{8\pi^2 r_0^2 a^3} \int \int_V \left(\frac{\sigma}{a} - 2 \right) \frac{e^{-\sigma/a}}{\sigma} d^3\mathbf{r} d^3\mathbf{r}', \quad (47)$$

where c_s is the surface-energy coefficient, $R_0 = r_0 A^{1/3}$, a is the surface diffuseness parameter, $\sigma = |\mathbf{r} - \mathbf{r}'|$, and V denotes the volume enclosed by the deformed nuclear surface. The latter has been defined in our study by means of the axial multipole expansion in terms of deformation parameters β_λ :

$$R(\Omega) = c(\beta) R_0 \left[1 + \sum_\lambda \beta_\lambda Y_{\lambda 0}(\Omega) \right] \quad (48)$$

with $c(\beta)$ being determined from the volume-conservation condition.

As demonstrated in Ref. [44], for small deformations the generalized surface energy, Eq. (47), is given to second order by

$$E_s = E_s(\text{sph}) + \sum_\lambda c_\lambda(\zeta) \beta_\lambda^2, \quad (49)$$

where the expansion coefficients c_λ solely depend on the dimensionless parameter

$$\zeta = \frac{R_0}{a} = \frac{r_0 A^{1/3}}{a}. \quad (50)$$

It can be shown [45] that the function $c_\lambda(\zeta)$ becomes negative below the critical value of ζ_c which is roughly proportional to the multipolarity λ . Consequently, the generalized surface energy is stable to β_λ if $\zeta > \zeta_c \approx 0.8\lambda$, or

$$a\lambda < R_0/0.8. \quad (51)$$

According to Eq. (51), for a given nucleus *both* large multipolarity *and* large diffuseness can trigger the shape instability. This conclusion also holds for the finite-range droplet model mass formula [45].

The weakly bound neutron-rich nuclei and halo systems are characterized by very diffused density distributions. For instance, it has been predicted in Ref. [15] that the average diffuseness in neutron drip-line nuclei can increase by as much as 50% as compared to the standard value representative of nuclei around the beta stability line. The effect of the large diffuseness on the macroscopic energy is illustrated in Fig. 14, which displays E_{macro} with the parameters of Ref. [46] for a light $A=20$ nucleus as a function of deformations β_2 , β_4 , and β_6 . Since at low deformations different multipolarities are decoupled, Eq. (49), they can be varied separately and the remaining ones are put to zero. The calculations are performed for three values of a . It is seen that the general rule given by Eq. (51) holds. Namely, for larger values of a and λ the macroscopic energy becomes unstable to shape deformation, mainly due to instability of E_s (for very light nuclei the effect of the Coulomb term is much weaker). Interestingly, the effect is fairly pronounced even for quadrupole distortions; the potential energy curve becomes unstable to β_2 already for $a=1.3a_{\text{std}}$. The above results indicate that in the microscopic-macroscopic approach both single-particle and macroscopic energy become extremely shallow to deformation for weakly bound systems.

V. CONCLUSIONS

In the limit of very weak binding, the geometric interpretation of shape deformation is lost. Consider, e.g., a deformed core with a prolate deformation and a weakly-bound halo neutron in a negative-parity orbital. According to the discussion above, the total quadrupole moment of the system diverges at the limit of vanishing binding (i.e., $\langle r^2 Y_{20} \rangle$ can take *any* value). On the other hand, depending on the geometry of the valence orbital, the total quadrupole deformation of the (core+valence) system is consistent with a superdeformed shape ($\pi=-$, $\Lambda=0$ halo) or oblate shape ($\pi=-$, $\Lambda=1$ halo). For a $\pi=+$ halo, the quadrupole moment is finite but β_2 approaches zero. In the language of the self-consistent mean-field theory, this result reflects the extreme softness of the system to the quadrupole distortion. Figure 15 shows an example of such a situation: The two valence particles occupying the weakly bound $[11-]$ orbital give rise to an oblate deformation of the system, in spite of the prolate deformation of the core and the prolate shape of the underlying spheroidal well ($\delta=0.2$).

Shape deformation is an extremely powerful concept provided that the nuclear surface can be properly defined. However, for very diffused and spatially extended systems the geometric interpretation of multipole moments and deformations is lost.

The presence of the spatially extended neutron halo gives rise to the presence of low-energy isovector modes in neutron-rich nuclei. The deformation decoupling of the halo implies that the nuclei close to the neutron drip line are excellent candidates for isovector quadrupole deformations, with different quadrupole deformations for protons and neutrons. Such nuclei are expected to have a very interesting rotational behavior and unusual magnetic properties. For instance, the rotational features of such systems (moments of inertia, $B(E2)$ values, g -factors) should be solely determined by the deformed core.

An example of the above scenario has been predicted in the self-consistent calculations for the neutron-rich sulfur isotopes performed using Skyrme Hartree-Fock and relativistic mean field methods [47,48]. When approaching the neutron drip line, the calculated values of β_2 for neutrons are systematically smaller than those of the proton distribution. This

example illustrates once again that in the drip-line nuclei, due to spatially extended wave functions, the “radial” contribution to the quadrupole moment might be as important as the “angular” part.

Finally, it is interesting to note that the anisotropic (non-spherical) halo systems have been investigated in molecular physics. A direct molecular analogy of a quadrupole-deformed halo nucleus is the electron weakly bound by the quadrupole moment of the neutral symmetric molecule such as CS₂ [35].

ACKNOWLEDGMENTS

This work has been supported by the U.S. Department of Energy through Contract No. DE-FG05-93ER40770. Oak Ridge National Laboratory is managed for the U.S. Department of Energy by Lockheed Martin Energy Research Corp. under Contract No. DE-AC05-96OR22464. The Joint Institute for Heavy Ion Research has as member institutions the University of Tennessee, Vanderbilt University, and the Oak Ridge National Laboratory; it is supported by the members and by the Department of Energy through Contract No. DE-FG05-87ER40361 with the University of Tennessee.

APPENDIX A: THE COMPUTATION OF SINGLE-PARTICLE WAVE FUNCTIONS

The amplitudes $A_{n_{\text{exc}}\Lambda l}$ and $B_{n_{\text{exc}}\Lambda l}$ in Eq. (40) can be found following the method outlined in Ref. [39]. The matching conditions for the internal and external wave functions (40) at $\xi = \xi_0$ lead to the following set of equations:

$$\sum_l^\infty A_{n_{\text{exc}}\Lambda l} R_{\Lambda l}^{(1)}(c_{\text{int}}, \xi_0) S_{\Lambda l}(c_{\text{int}}, \eta) = \sum_l^\infty B_{n_{\text{exc}}\Lambda l} R_{\Lambda l}^{(3)}(ic_{\text{ext}}, \xi_0) S_{\Lambda l}(ic_{\text{ext}}, \eta) \quad (\text{A1})$$

and

$$\sum_l^\infty A_{n_{\text{exc}}\Lambda l} \left(\frac{dR_{\Lambda l}^{(1)}(c_{\text{int}}, \xi)}{d\xi} \right)_{\xi_0} S_{\Lambda l}(c_{\text{int}}, \eta) = \sum_l^\infty B_{n_{\text{exc}}\Lambda l} \left(\frac{dR_{\Lambda l}^{(3)}(ic_{\text{ext}}, \xi)}{d\xi} \right)_{\xi_0} S_{\Lambda l}(ic_{\text{ext}}, \eta). \quad (\text{A2})$$

The matching conditions [Eqs. (A1) and (A2)] should hold for any value of η . To eliminate this degree of freedom, one can take advantage of the fact that the angular spheroidal functions $S_{\Lambda l}(c, \eta)$ form a complete orthogonal set in the interval $-1 \leq \eta \leq 1$. By multiplying both sides of Eqs. (A1) and (A2) by $S_{\Lambda l'}^*(ic_{\text{ext}}, \eta)$ and integrating over η , one obtains the matrix equation for $A_{n_{\text{exc}}\Lambda l}$:

$$\sum_l^\infty A_{n_{\text{exc}}\Lambda l} M_{ll'} = 0 \quad \text{for all } l', \quad (\text{A3})$$

where

$$M_{ll'} \equiv \left\{ \left(\frac{dR_{\Lambda l}^{(1)}(c_{\text{int}}, \xi)}{d\xi} \right)_{\xi_0} R_{\Lambda l'}^{(3)}(ic_{\text{ext}}, \xi_0) - \left(\frac{dR_{\Lambda l'}^{(3)}(ic_{\text{ext}}, \xi)}{d\xi} \right)_{\xi_0} R_{\Lambda l}^{(1)}(c_{\text{int}}, \xi_0) \right\} \times \langle S_{\Lambda l'}(ic_{\text{ext}}) | S_{\Lambda l}(c_{\text{int}}) \rangle. \quad (\text{A4})$$

The eigenenergies $\epsilon_{n_{\text{exc}}\Lambda\pi}$ and the corresponding amplitudes $A_{n_{\text{exc}}\Lambda l}$ are found from the condition that $\det(M)=0$.

APPENDIX B: SEPARATION OF THE SCHRÖDINGER EQUATION

In the limit of very small binding energy and/or large deformations, particular attention should be paid to the numerical method employed for determining the separation constant $\lambda_{\Lambda l}$ [Eq. (34)] and amplitudes $d_k^{\Lambda l}$ appearing in Eqs. (38) and (39).

The separation constant $\lambda_{\Lambda l}$ and coefficients $d_k^{\Lambda l}(c)$ can be obtained from the three-term recurrence formula [40]:

$$\begin{aligned} & \left[\frac{k(k-1)}{(2k+2\Lambda-1)(2k+2\Lambda-3)} \right] d_{k-2}^{\Lambda l} + \left[\frac{(k+2\Lambda+1)(k+2\Lambda+2)}{(2k+2\Lambda+3)(2k+2\Lambda+5)} \right] d_{k+2}^{\Lambda l} \\ & + \left[\frac{2(k+\Lambda)(k+\Lambda+1)-2\Lambda^2-1}{(2k+2\Lambda+3)(2k+2\Lambda-1)} + \frac{(k+\Lambda)(k+\Lambda+1)-\lambda_{\Lambda l}}{c^2} \right] d_k^{\Lambda l} = 0. \end{aligned} \quad (\text{B1})$$

It is interesting to note that for $c \rightarrow 0$ [the last term in Eq. (B1) dominates] $l=\ell$, the separation constant becomes $\lambda_{\Lambda l} = \ell(\ell+1)$, and the only nonvanishing coefficient corresponds to $k=\ell-\Lambda$. That is, the wave functions (38) and (39) are those of the *spherical* well. Indeed, according to Eq. (37), the limit of $c \rightarrow 0$ is reached at the spherical shape ($a \rightarrow 0$). However, the limit of $c_{\text{ext}} \rightarrow 0$ is also approached at *deformed shapes* if the binding energy is small.

By defining

$$\alpha_k \equiv d_{k-\Lambda} / \sqrt{\frac{2k+1}{2} \frac{(k-\Lambda)!}{(k+\Lambda)!}}, \quad (\text{B2})$$

the matrix equation (B1) can be reduced to the Hermitian eigenvalue problem [39]

$$\begin{aligned} \lambda_{\Lambda l}(c)\alpha_k &= \frac{c^2}{2k+3} \sqrt{\frac{(k+\Lambda+1)(k+\Lambda+2)(k-\Lambda+1)(k-\Lambda+2)}{(2k+1)(2k+5)}} \alpha_{k+2} \\ &+ \left\{ k(k+1) + c^2 \frac{2k(k+1)-2\Lambda^2-1}{(2k+3)(2k-1)} \right\} \alpha_k \\ &+ \frac{c^2}{2k-1} \sqrt{\frac{(k+\Lambda-1)(k+\Lambda)(k-\Lambda-1)(k-\Lambda)}{(2k-3)(2k+1)}} \alpha_{k-2}. \end{aligned} \quad (\text{B3})$$

Another way of computing $\lambda_{\Lambda l}$ and $d_k^{\Lambda l}$ is to employ the recurrence relations for the ratio d_k/d_{k-2} [42,41]:

$$\frac{d_{k+2}}{d_k} + \beta_k + \gamma_k \left(\frac{d_k}{d_{k-2}} \right)^{-1} = 0, \quad (\text{B4})$$

where β_k and γ_k can be expressed through factors appearing in Eq. (B1).

The technique based on the recurrence relation (B4) is useful when calculating radial wave functions at large deformations. In general, the coefficients d_k are largest in magnitude at $k = l - \Lambda$, and quickly decrease with k . On the other hand, the magnitudes of

spherical Bessel functions of the third kind, $h_k(ic\xi)$, rapidly increase with k . Consequently, the product $d_k^{\Lambda}(c)h_{k+\Lambda}(ic\xi)$ becomes numerically unstable at large values of k if d_k and $h_{k+\Lambda}$ are computed separately. This problem can be overcome by writing the recurrence relation (B4) in the form

$$\left(\frac{d_{k+2}h_{k+\Lambda+2}}{d_k h_{k+\Lambda}}\right) \left(\frac{h_{k+\Lambda+2}}{h_{k+\Lambda}}\right)^{-1} + \beta_k + \gamma_k \left(\frac{d_k h_{k+\Lambda}}{d_{k-2} h_{k+\Lambda-2}}\right)^{-1} \left(\frac{h_{k+\Lambda}}{h_{k+\Lambda-2}}\right) = 0 \quad (\text{B5})$$

and employing the property of Bessel functions $h_k(iz)$

$$\frac{h_{k+2}}{h_k} + 1 + \frac{2k+3}{z} \left[\frac{2k+1}{z} + \frac{z}{2k-1} \left\{ 1 + \left(\frac{h_k}{h_{k-2}}\right)^{-1} \right\} \right] = 0. \quad (\text{B6})$$

REFERENCES

- [1] H. Geissel, G. Münzenberg, and K. Riisager, *Annu. Rev. Nucl. Part. Sci.* **45**, 163 (1995).
- [2] A. Mueller and B. Sherril, *Annu. Rev. Nucl. Part. Sci.* **43**, 529 (1993).
- [3] K. Riisager, *Rev. Mod. Phys.* **66**, 1105 (1994).
- [4] P.G. Hansen, A.S. Jensen, and B. Jonson, *Annu. Rev. Nucl. Part. Phys.* **45**, 591 (1995).
- [5] I. Tanihata, *Jour. of Phys. G* **22**, 157 (1996).
- [6] E.P. Wigner, *Phys. Rev.* **73**, 1002 (1948).
- [7] U. Fano, *Phys. Rev.* **124**, 1866 (1961).
- [8] T. Uchiyama and H. Morinaga, *Z. Phys.* **A320**, 273 (1985).
- [9] S.A. Fayans, *Phys. Lett.* **B267**, 443 (1991).
- [10] M. Yokoyama, T. Otsuka, and N. Fukunishi, *Phys. Rev.* **C52**, 1122 (1995).
- [11] H. Sagawa, N. Van Giai, N. Takigawa, M. Ishihara, and K. Yazaki, *Z. Phys.* **A351**, 385 (1995).
- [12] I. Hamamoto, H. Sahawa, and X.Z. Zhang, *Phys. Rev.* **C53**, 765 (1996).
- [13] F. Tondeur, *Z. Phys.* **A288**, 97 (1978).
- [14] D. Hirata, H. Toki, T. Watabe, I. Tanihata, and B.V. Carlson, *Phys. Rev.* **C44**, 1467 (1991).
- [15] J. Dobaczewski, I. Hamamoto, W. Nazarewicz, and J.A. Sheikh, *Phys. Rev. Lett.* **72**, 981 (1994).
- [16] J. Dobaczewski, W. Nazarewicz, T.R. Werner, J.-F. Berger, C.R. Chinn, and J. Dechargé, *Phys. Rev.* **C53**, 2809 (1996).
- [17] M. Fukuda, T. Ichihara, N. Inabe, T. Kubo, H. Kumagai, T. Nakagawa, Y. Yano, I. Tanihata, M. Adachi, K. Asahi, M. Kouguchi, M. Ishihara, H. Sagawa, and S. Shimoura, *Phys. Lett.* **B 268**, 339 (1991).
- [18] S. Raman, C.H. Malarkey, W.T. Milner, C.W. Nestor, Jr., and P.H. Stelson, *Atomic Data Nucl. Data Tables* **36** (1987) 1.
- [19] T. Minamisono, T. Ohtsubo, I. Minami, A. Kitagawa, M. Fukuda, K. Matsuta, Y. Nojiri, S. Takeda, H. Sagawa, and H. Kitagawa, *Phys. Rev. Lett.* **69**, 2058 (1992).
- [20] H. Nakada and T. Otsuka, *Phys. Rev.* **C49**, 886 (1994).
- [21] M. Bouten, E. Flerackers, and M.C. Bouten, *Nucl. Phys.* **A307**, 413 (1978).
- [22] I. Ragnarsson, S. Åberg, H.-B. Håkansson, and R.K. Sheline, *Nucl. Phys.* **A361**, 1 (1981).
- [23] A. Muta and T. Otsuka, preprint 1995.
- [24] T. Otsuka, A. Muta, M. Yokoyama, N. Fukunishi, and T. Suzuki, *Nucl. Phys.* **A588**, 113c (1995).
- [25] I. Tanihata, D. Hirata, and H. Toki, *Nucl. Phys.* **A583**, 769 (1995).
- [26] I. Tanihata, T. Kobayashi, O. Yamakawa, S. Shimoura, K. Ekuni, K. Sugimoto, N. Takahashi, T. Shimoda, and H. Sato, *Phys. Lett.* **B206**, 592 (1988).
- [27] Y. Kanada-Enyo, H. Horiuchi, and A. Ono, *Phys. Rev.* **C52**, 628 (1995).
- [28] X. Li and P.-H. Heenen, *Phys. Rev.* **54**, 1617 (1996).
- [29] H. Esbensen, B.A. Brown, and H. Sagawa, *Phys. Rev.* **C51**, 1274 (1995).
- [30] N. Vinh Mau, *Nucl. Phys.* **A592**, 33 (1995).
- [31] C.A. Bertulani and H. Sagawa, *Nucl. Phys.* **A588**, 667 (1995).
- [32] F.M. Nunes, I.J. Thompson, and R.C. Johnson, *Nucl. Phys.* **A596**, 171 (1996).
- [33] D. Ridikas and J.S. Vaagen, Preprint ETC*-96-006, 1996.

- [34] W.R. Garrett, Phys. Rev. **A3**, 961 (1971).
- [35] R.N. Compton, F.B. Dunning, and P. Norlander, Chem. Phys. Lett. **253**, 8 (1996).
- [36] K. Riisager, A.S. Jensen, and P. Møller, Nucl. Phys. **A548**, 393 (1992).
- [37] D.V. Fedorov, A.S. Jensen, and K. Riisager, Phys. Lett. **B 312**, 1 (1993).
- [38] S.A. Moszkowski, Phys. Rev. **99**, 803 (1955).
- [39] A.C. Merchant and W.D.M. Rae, Nucl. Phys. **A571**, 43 (1994).
- [40] P.M. Morse and H. Feshbach, *Methods of Theoretical Physics* (McGraw-Hill, New York, 1953).
- [41] J.D. Little and F.J. Corbató, in *Spheroidal Wave Functions*, ed. by J.A. Stratton (Wiley, New York, 1956), p. 53.
- [42] *Handbook of Mathematical Functions*, ed. by M. Abramowitz and I. Stegun (Dover, New York, 1965).
- [43] W. Nazarewicz and I. Ragnarsson, in: *Handbook of Nuclear Properties*, ed. by D.N. Poenaru and W. Greiner (Clarendon Press, Oxford, 1996), p. 80.
- [44] H.J. Krappe, J.R. Nix, and A.J. Sierk, Phys. Rev. **C20**, 992 (1979).
- [45] L.-O. Jönsson, Nucl. Phys. **A608**, 1 (1996).
- [46] P. Möller and J.R. Nix, At. Data Nucl. Data Tables **39** (1988) 213.
- [47] T.R. Werner, J.A. Sheikh, W. Nazarewicz, M.R. Strayer, A.S. Umar, and M. Misu, Phys. Lett. **B333**, 303 (1994).
- [48] T.R. Werner, J.A. Sheikh, M. Misu, W. Nazarewicz, J. Rikovska, K. Heeger, A.S. Umar, and M.R. Strayer, Nucl. Phys. **A597**, 327 (1996).

FIGURES

FIG. 1. Nuclear rms radii calculated in the modified harmonic oscillator model (squares) for a series of Be isotopes. They are compared to measured [26] interaction radii (open circles). The calculated deviation from the smooth $1.1A^{1/3}$ behavior (dot-dash line) is due to deformation.

FIG. 2. Shapes corresponding to quadrupole deformations $\delta=0, 0.2, 0.6,$ and $1.2,$ assuming the volume conservation condition, Eq. (29).

FIG. 3. Single-particle energies of the finite spheroidal well with $U_0=-80$ MeV and $R_0=4$ fm as a function of deformation δ . At a spherical shape the orbitals are characterized by means of quantum numbers ($n\ell$). The deformed orbitals are labeled by parity ($\pi=+$, solid line; $\pi=-$, dashed line) and by orbital angular momentum projection onto the symmetry axis (z -axis), Λ .

FIG. 4. Dependence of the single-particle rms radius on binding energy ϵ at $\delta=0$ (spherical shape) and $R_0=4$ fm. The potential depth is adjusted in each case to obtain the desired value of ϵ . The values of $\langle r^2 \rangle$ for $1s$ and $1p$ orbitals diverge at small binding energies according to the power law, Eq. (17).

FIG. 5. Binding energy dependence of $\langle r^2 \rangle$ (solid line), $\langle r^2 Y_{20} \rangle$ (dashed line), and β_2 (dotted line) for several $\pi=+$ orbitals at $\delta=0.6$ (superdeformed shape). The asymptotic limits discussed in Sec. II are indicated.

FIG. 6. Same as in Fig. 5 except for the $\pi=-$ states.

FIG. 7. Probability P_{outer} , Eq. (15), to find the neutron in the classically forbidden region, $\xi > \xi_0$, as a function of ϵ for three superdeformed states $[12+]$, $[21-]$, and $[20+]$.

FIG. 8. Radial form factors, Eq. (41), for several $\pi=+$ orbitals in a superdeformed well ($\delta=0.6$, $R_0=4$ fm) at the “subthreshold” binding energy $\epsilon=-5$ keV. The probability $P_\ell(\Lambda n_{\text{exc}})$, Eq. (42), is indicated.

FIG. 9. Same as in Fig. 8 except for $\pi=-$ orbitals.

FIG. 10. Contour maps of probabilities P_0 and P_2 , Eq. (42), for the $[10+]$ (top) and $[20+]$ (bottom) levels as functions of deformation δ and binding energy ϵ . Calculations were performed for $R_0=4$ fm.

FIG. 11. Same as in Fig. 10 except for probabilities P_1 and P_3 for the $[10-]$ (top) and $[20-]$ (bottom) levels.

FIG. 12. Quadrupole deformation β_2 of the valence orbital (dotted line), that of the core (dashed line), and the total quadrupole deformation of the system (solid line) as a function of the binding energy of the indicated valence orbital of positive parity. Calculations were performed for $R_0=4$ fm and $\delta=0.6$.

FIG. 13. Same as in Fig. 12 except for $\pi=-$ valence orbitals.

FIG. 14. The macroscopic energy, E_{macro} , for $Z=N=10$ (normalized to zero at spherical shape) given by the Yukawa-plus-exponential mass formula as a function of β_2 (top), β_4 (middle), and β_6 (bottom) for three values of surface diffuseness: $a_{\text{std}}=0.68$ fm (solid line), $a=1.3a_{\text{std}}$ (dashed line), and $a=1.5a_{\text{std}}$ (dotted line). It is seen that the macroscopic energy develops deformation instability with *both* increasing diffuseness and the multipolarity of deformation.

FIG. 15. Contour plot (in logarithmic scale) of the ρr^2 distribution in the (x, z) -plane. Here, ρ denotes the single-particle density, i.e., $\rho(\mathbf{r})=\sum_{\nu-\text{occ.}} |\psi_{\nu}(\mathbf{r})|^2$. The deformation of the spheroidal well is assumed to be $\delta=0.2$ and the corresponding prolate shape is indicated by a dashed line. Left: distribution for a core consisting of $N=4$ particles (counting from the bottom of the well). Right: ρr^2 distribution for the $N=6$ system. The two valence orbitals occupy the weakly bound $\epsilon=-5$ keV [11-] orbital.

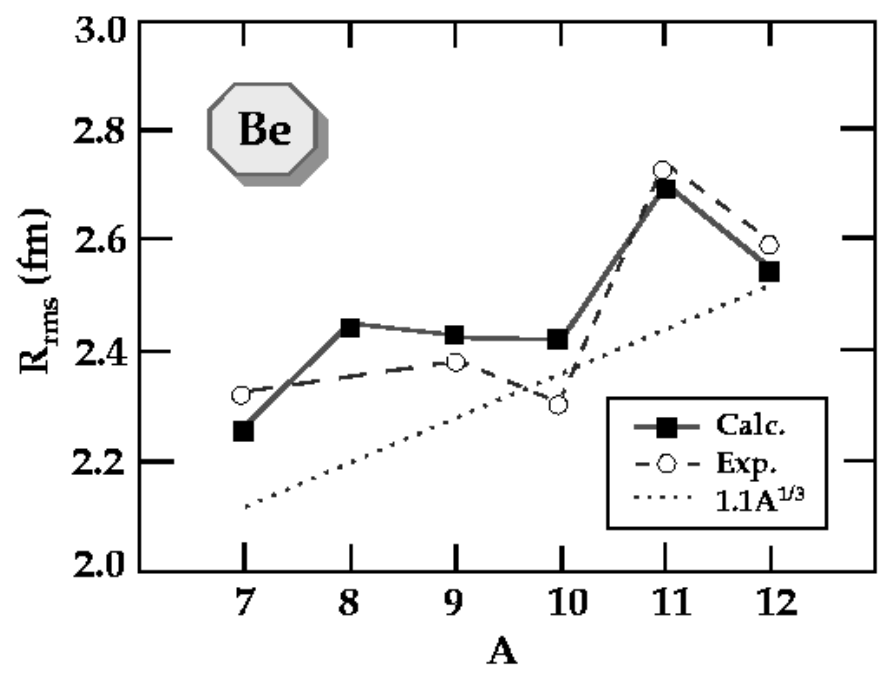


FIG.1

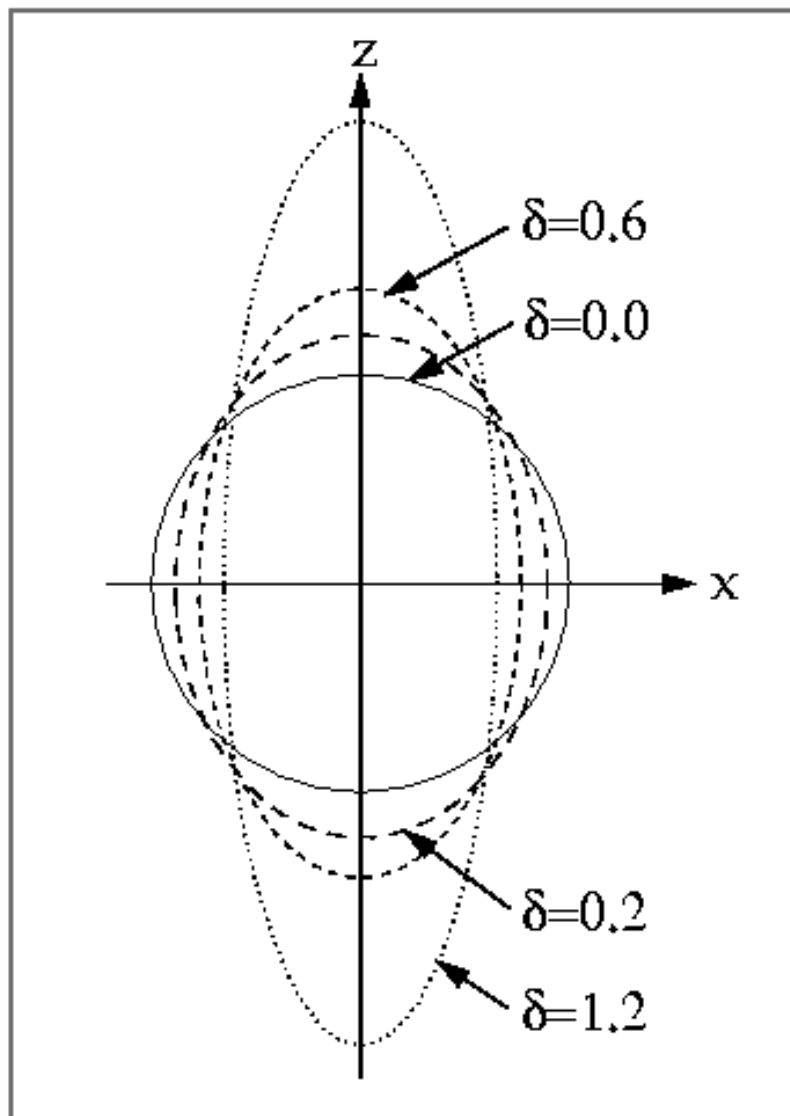


FIG.2

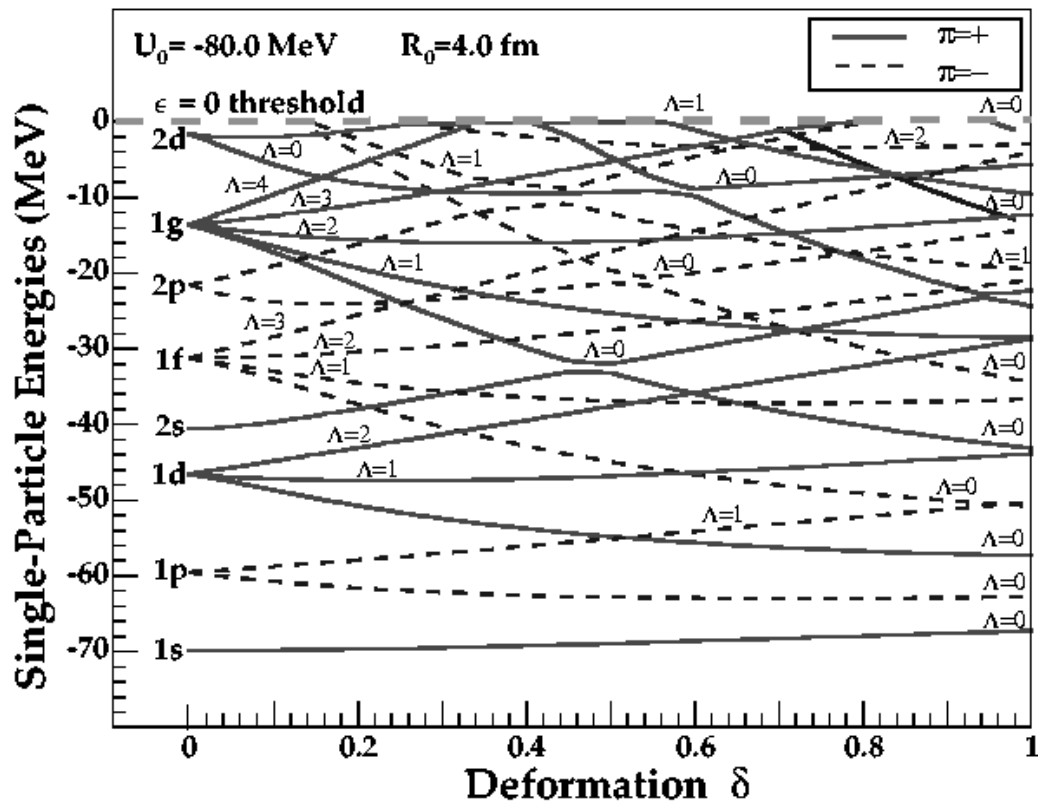


FIG.3

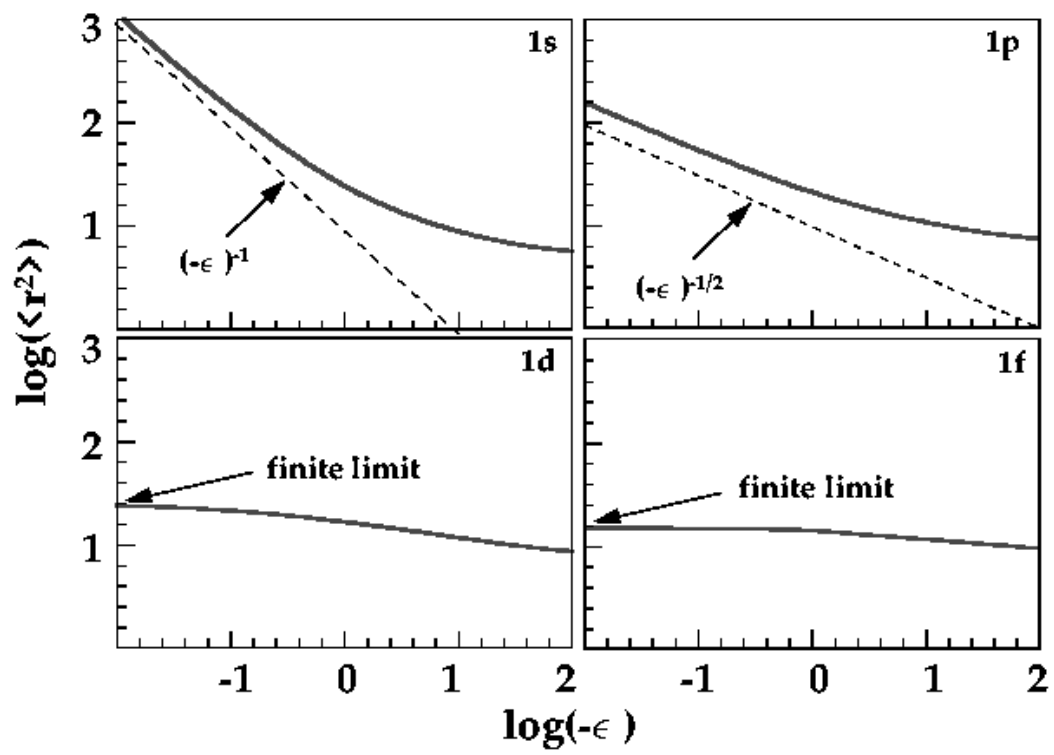


FIG.4

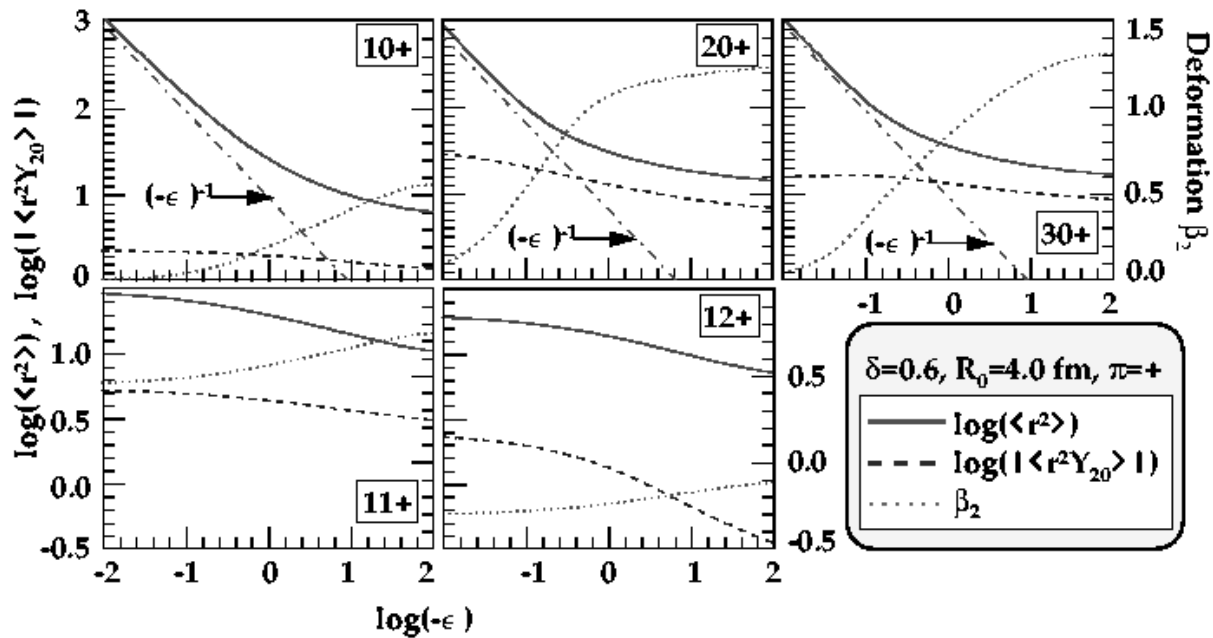


FIG.5

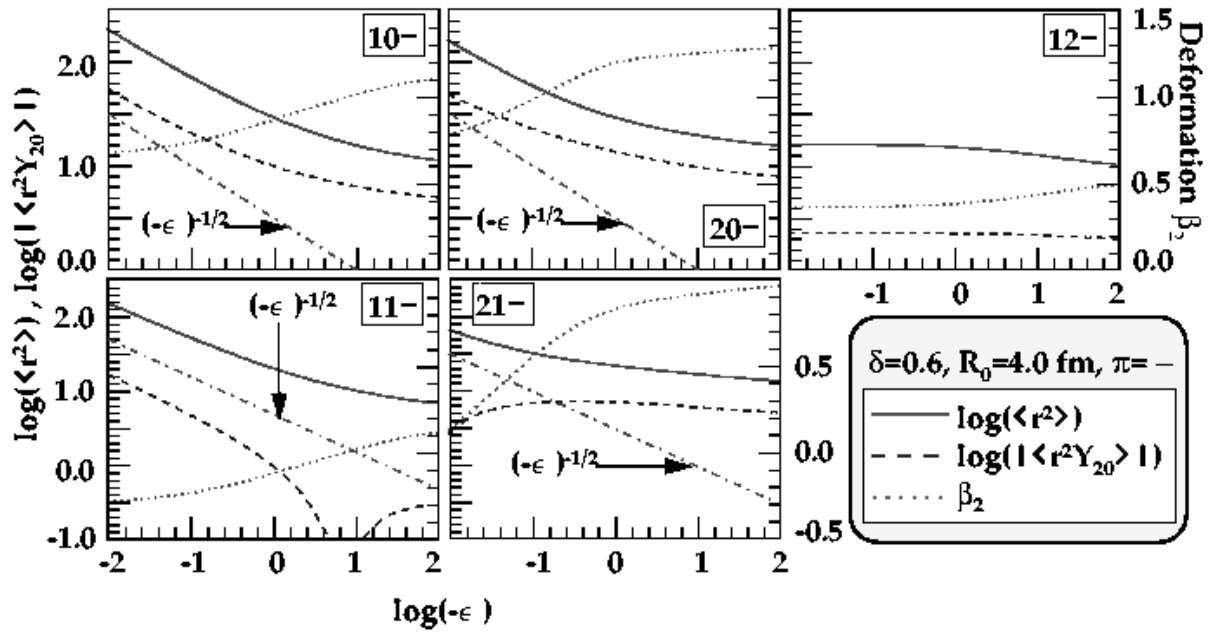


FIG.6

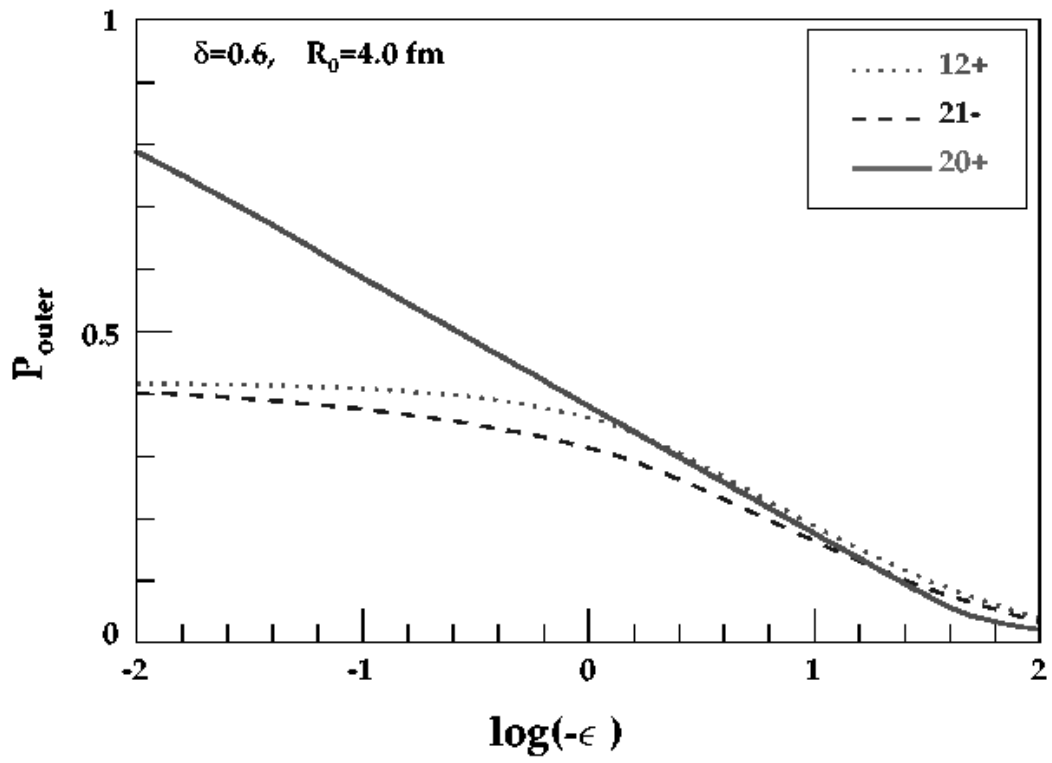


FIG.7

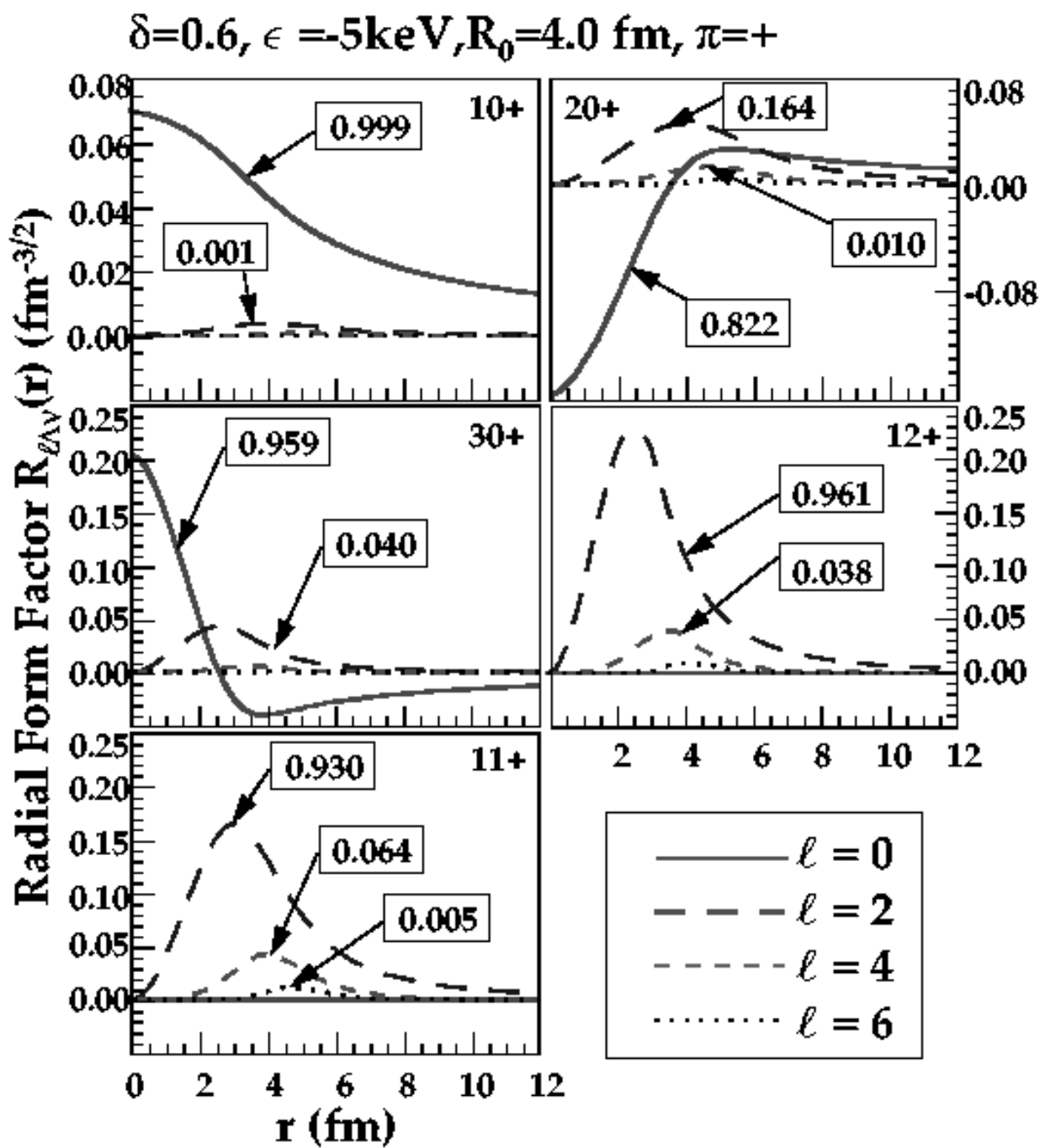


FIG.8

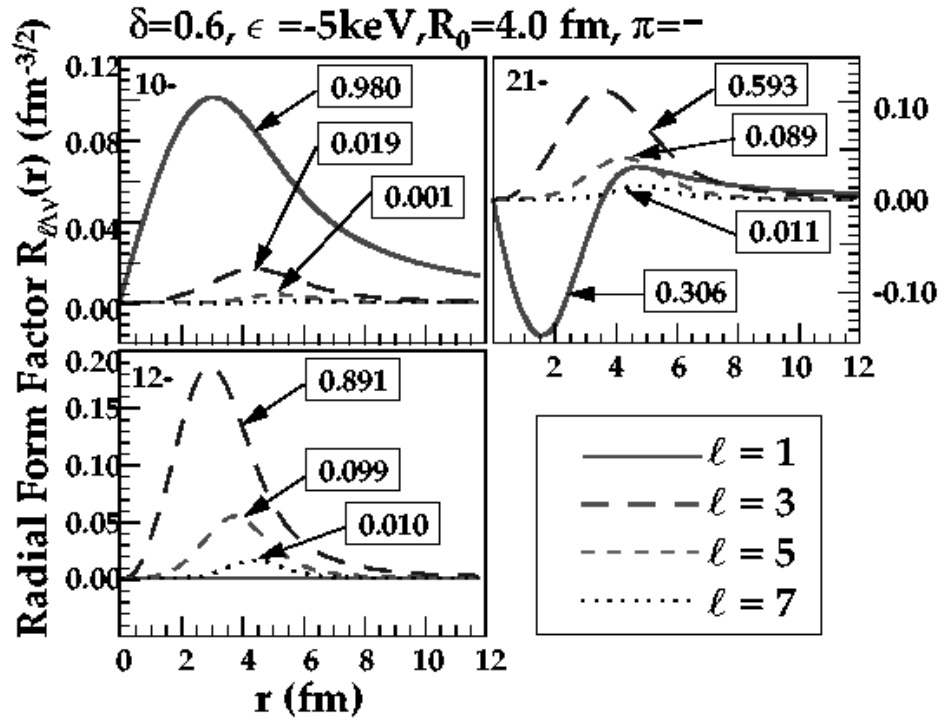


FIG.9

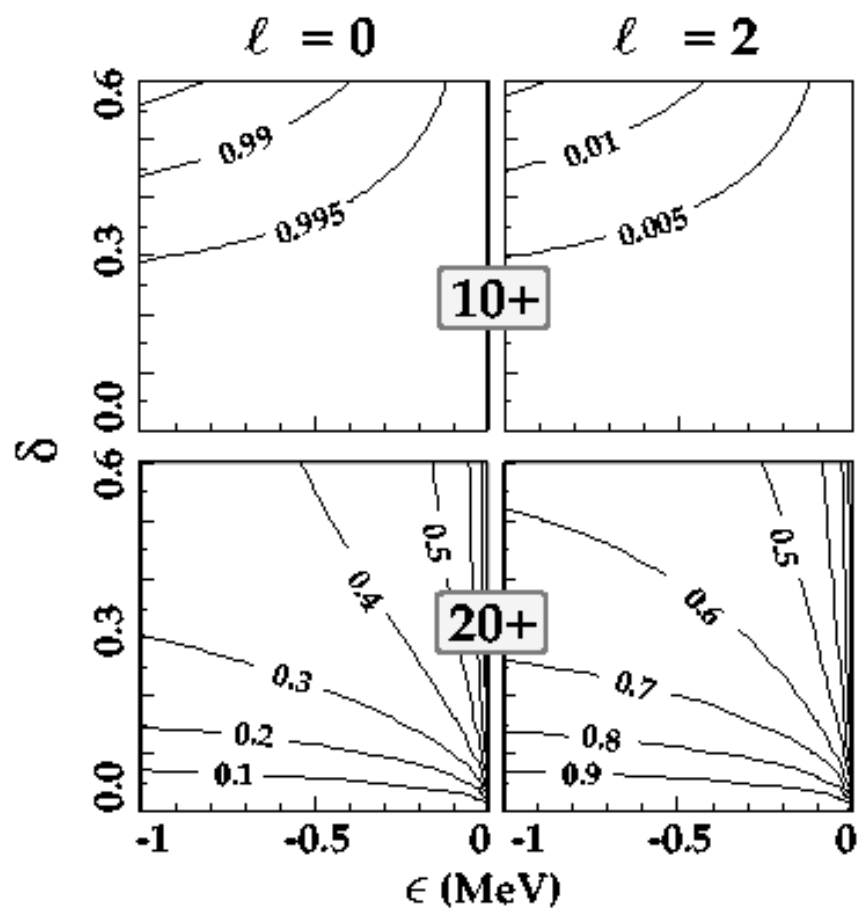


FIG.10

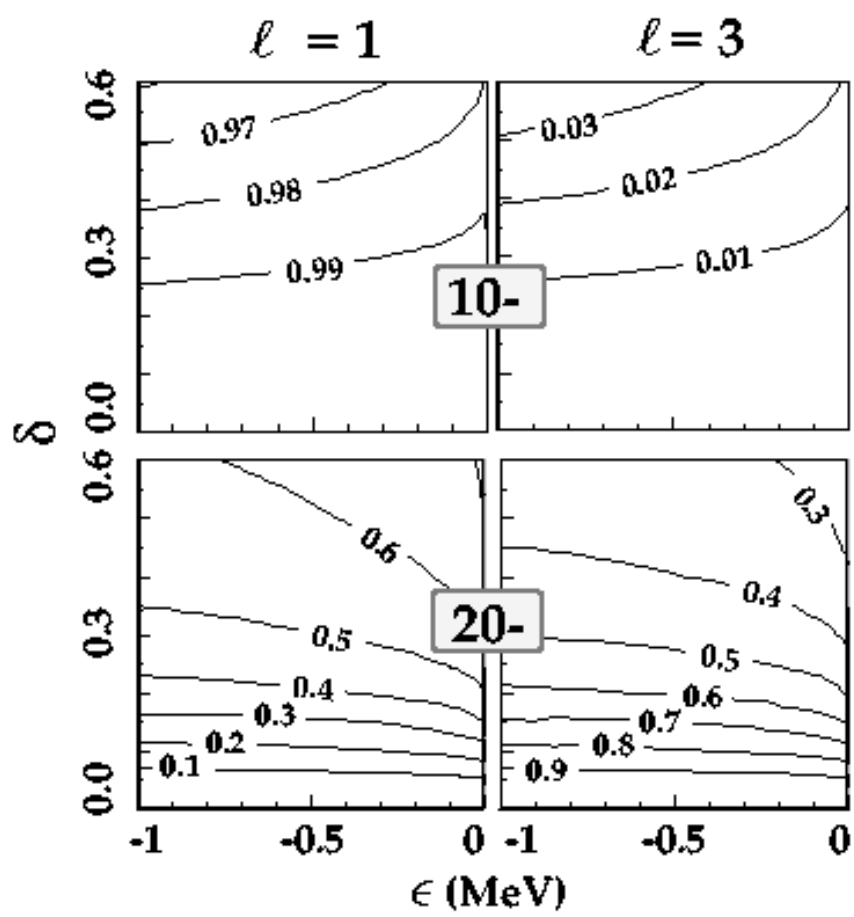


FIG.11

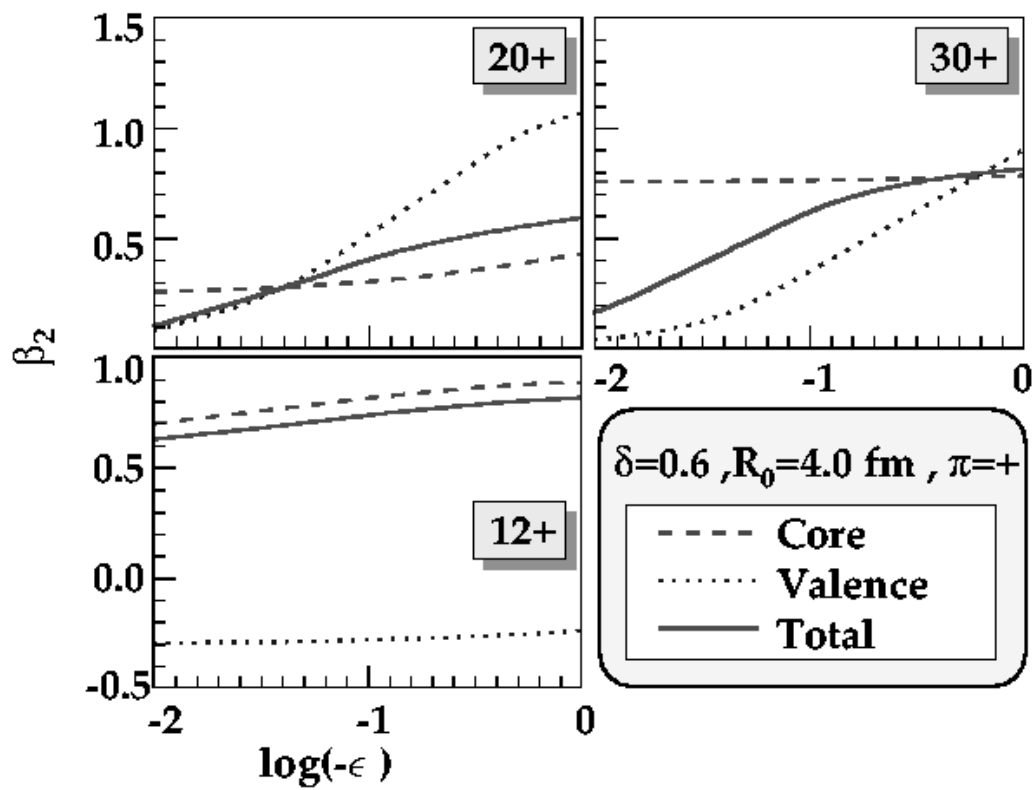


FIG.12

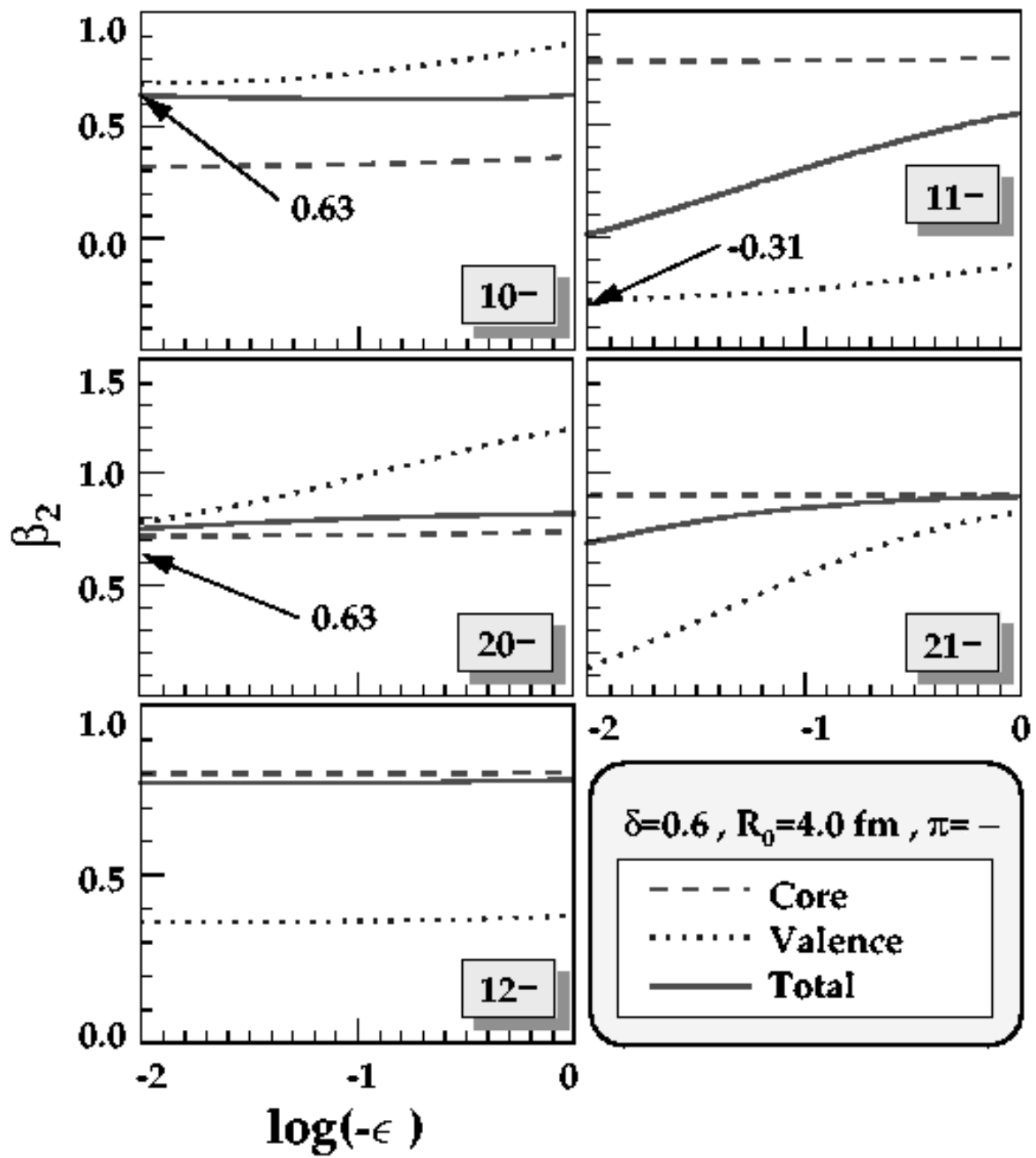


FIG.13

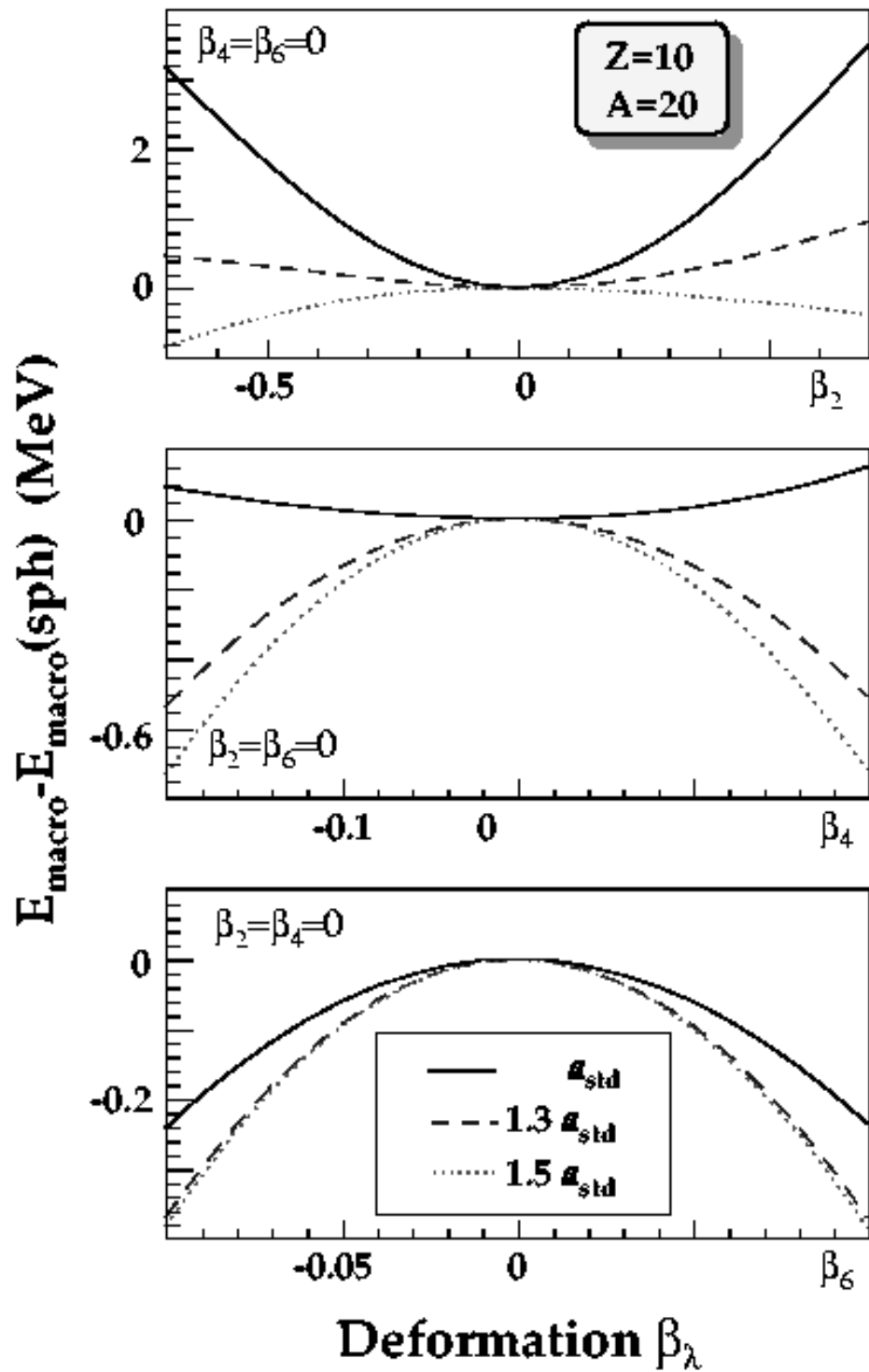


FIG.14

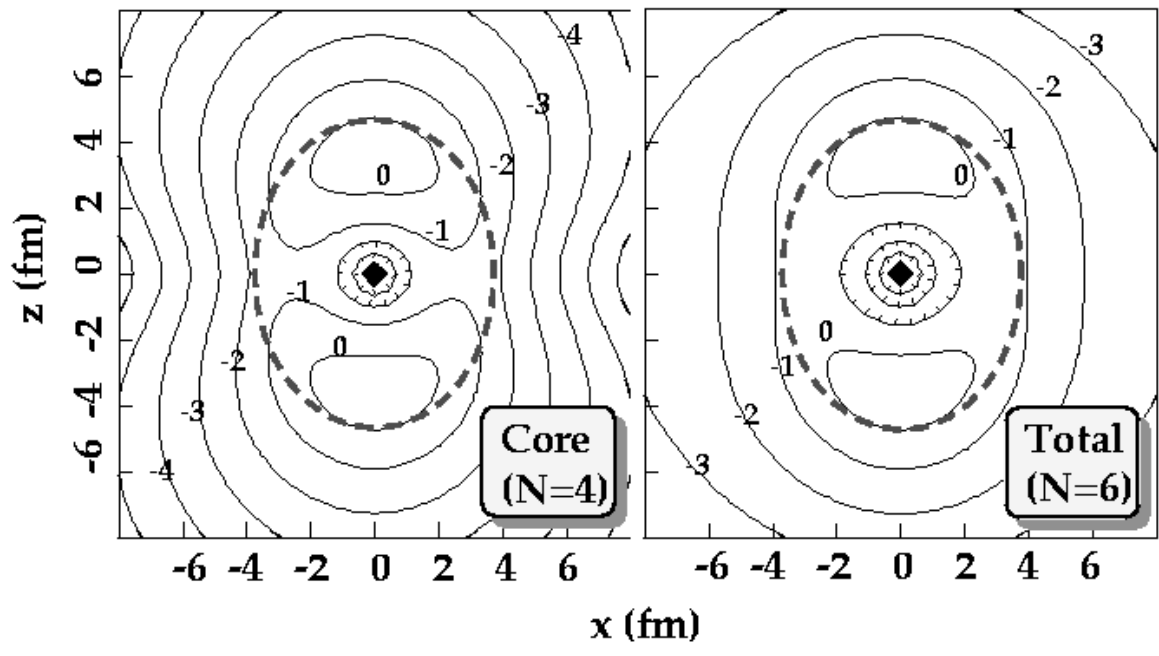


FIG.15